Title
Correlation-driven electronic reconstruction in FeTe1−xSex

Journal
Communications Physics, 5(1)

ISSN
2399-3650

Authors
Huang, Jianwei
Yu, Rong
Xu, Zhijun
et al.

Publication Date
2022

DOI
10.1038/s42005-022-00805-6

Peer reviewed

communications physics

ARTICLE

https://doi.org/10.1038/s42005-022-00805-6 OPEN

Correlation-driven electronic reconstruction in $FeTe_{1-x}Se_x$

Jianwei Huang[1], Rong Yu[2], Zhijun Xu[3,4,5], Jian-Xin Zhu[6,7], Ji Seop Oh[1,5], Qianni Jiang[8], Meng Wang[9], Han Wu[1], Tong Chen[1], Jonathan D. Denlinger[10], Sung-Kwan Mo[10], Makoto Hashimoto[11], Matteo Michiardi[12,13,14], Tor M. Pedersen[15], Sergey Gorovikov[15], Sergey Zhdanovich[12,13], Andrea Damascelli[12,13], Genda Gu[16], Pengcheng Dai[1], Jiun-Haw Chu[8], Donghui Lu[11], Qimiao Si[1], Robert J. Birgeneau[5,17,18]✉ & Ming Yi[1,5]✉

Electronic correlation is of fundamental importance to high temperature superconductivity. While the low energy electronic states in cuprates are dominantly affected by correlation effects across the phase diagram, observation of correlation-driven changes in fermiology amongst the iron-based superconductors remains rare. Here we present experimental evidence for a correlation-driven reconstruction of the Fermi surface tuned independently by two orthogonal axes of temperature and Se/Te ratio in the iron chalcogenide family $FeTe_{1-x}Se_x$. We demonstrate that this reconstruction is driven by the de-hybridization of a strongly renormalized d_{xy} orbital with the remaining itinerant iron 3*d* orbitals in the emergence of an orbital-selective Mott phase. Our observations are further supported by our theoretical calculations to be salient spectroscopic signatures of such a non-thermal evolution from a strongly correlated metallic phase into an orbital-selective Mott phase in d_{xy} as Se concentration is reduced.

[1] Department of Physics and Astronomy, Rice Center for Quantum Materials, Rice University, Houston, TX 77005, USA. [2] Department of Physics, Renmin University of China, 100872 Beijing, China. [3] NIST Center for Neutron Research, National Institute of Standards and Technology, Gaithersburg, MD 20899, USA. [4] Department of Materials Science and Engineering, University of Maryland, College Park, MD 20742, USA. [5] Department of Physics, University of California Berkeley, Berkeley, CA 94720, USA. [6] Theoretical Division, Los Alamos National Laboratory, Los Alamos, NM 87545, USA. [7] Center for Integrated Nanotechnologies, Los Alamos National Laboratory, Los Alamos, NM 87545, USA. [8] Department of Physics, University of Washington, Seattle, WA 98195, USA. [9] School of Physics, Sun Yat-sen University, Guangzhou 510275 Guangdong, China. [10] Advanced Light Source, Lawrence Berkeley National Lab, Berkeley, CA 94720, USA. [11] Stanford Synchrotron Radiation Lightsource, SLAC National Accelerator Laboratory, Menlo Park, CA 94025, USA. [12] Department of Physics & Astronomy, University of British Columbia, Vancouver, BC V6T 1Z1, Canada. [13] Quantum Matter Institute, University of British Columbia, Vancouver, BC V6T 1Z4, Canada. [14] Max Planck Institute for Chemical Physics of Solids, Nöthnitzer Straße 40, 01187 Dresden, Germany. [15] Canadian Light Source, Inc., 44 Innovation Boulevard, Saskatoon, SK S7N 2V3, Canada. [16] Condensed Matter Physics and Materials Science Department, Brookhaven National Laboratory, Upton, NY 11973, USA. [17] Materials Sciences Division, Lawrence Berkeley National Laboratory, Berkeley, CA 94720, USA. [18] Department of Materials Science and Engineering, University of California Berkeley, Berkeley, CA 94720, USA. ✉email: robertjb@berkeley.edu; mingyi@rice.edu

The phase diagrams of the copper oxide superconductors and iron-based superconductors (FeSCs) have often been compared to demonstrate a degree of similarity—a superconducting dome emerging from the suppression of a magnetic ground state[1–3]. Electron correlations as well as effects of symmetry-breaking electronic orders have been observed in both[3–6]. However, the dominant mechanism that drives the evolution of the Fermi surface and low energy quasiparticles differs in the two material systems. In the cuprates, the parent compound is an antiferromagnetic (AFM) Mott insulator, from which low energy quasiparticles emerge as the system is doped away from half-filling, eventually approaching a Fermi liquid on the overdoped side[4,7]. In most FeSCs, the parent compound is a metal harboring a spin-density wave order[8], where the Fermi surface is well-defined and can be largely understood as a modified version of the non-magnetic fermiology reconstructed by the symmetry-breaking electronic orders[9]. Therefore, while arguably the dominant mechanism that controls the evolution of the fermiology in the cuprates is electron correlation effects, that for the FeSCs have largely been understood to be the symmetry-breaking electronic orders[6,10].

However, it has also been recognized early on that the FeSCs exhibit moderate correlations[5]. The analysis of the experimentally observed Drude weight from optical conductivity puts the FeSCs between the limits of the Mott insulator and the itinerant metal[11]. Moreover, from both theory and experimental observation via angle-resolved photoemissoin spectroscopy (ARPES), it has been recognized that such correlations are orbital-dependent[5,6,12,13]. In particular, while the FeSCs as bad metals are deemed to be moderately correlated compared to the cuprate high temperature superconductors, the electrons belonging to different orbitals are found to be correlated to different degrees—stronger in the d_{xy} orbital than in the d_{xz}/d_{yz} orbitals[6]. This orbital-differentiation is enhanced by Hund's coupling, and increases systematically in sync with the vertical elongation of the iron tetrahedron from the iron-phosphides to iron-pnictides to iron-chalcogenides[6], in which strong orbital-selectivity has been reported[14–16]. From the electronic degree of freedom, the effective mass of the d_{xy} orbital dominated band has been reported to be larger than that of the d_{xz}/d_{yz} orbitals. From both the nuclear magnetic resonance and neutron scattering measurements, coexistence of both itinerant and local spins has been found[17], where the d_{xy} orbital contributes dominantly to the local spin susceptibility[18–20]. As an example, inelastic neutron scattering experiments on detwinned NaFeAs, a parent compound of FeSCs, have shown that spin waves of the system are orbital-selective with high energy spin waves arising mostly from the d_{xy} orbital and obeying the C_4 rotational symmetry, while the low energy spin waves are from the d_{xz}/d_{yz} orbitals that break the C_4 rotational symmetry below the nematic phase transition temperature[21,22].

A question then arises—while the fermiology of the FeSCs is far from that of a Mott insulator, could the strong localization of a selective orbital be sufficient to induce significant modifications to the fermiology and associated low energy electronic states?

Generically in a multiorbital material, this can be realized in an orbital-selective Mott phase (OSMP), where selected orbitals can become completely localized and gapped out from the Fermi level while other orbitals maintain a degree of itinerancy[5,12,23–27]. As the system evolves into an OSMP, the hybridization between the electrons belonging to the strongly localized orbitals and the itinerant orbitals gradually turns off, leading to a reconstruction of the fermiology. In the larger context of quantum materials, evidence for OSMP has been reported for $Ca_{2-x}Sr_xRuO_4$[28–30], VO_2[31], and a transition metal dichalcogenide[32], in the form of strongly orbital-selective mass enhancement and spectral weight gapped out at the Fermi level[29,33–37]. However, continuous evolution of Fermi surface reconstruction across an OSMP has been challenging to show for any material system, and has only recently been reported for $Ca_{2-x}Sr_xRuO_4$[30].

In this context, the strongly correlated iron-chalcogenide materials provide an opportunity to realize such correlation-driven Fermi surface reconstruction. To examine this, we consider the regime where evidence for a thermal crossover into an OSMP has recently been reported in $FeTe_{1-x}Se_x$[15,38]. In these prior works, the d_{xy} orbital is strongly renormalized at low temperatures and loses spectral weight as temperature is raised sufficiently high[15,38]. To examine the effect of such strong correlations on the fermiology, it is desired to go beyond the study of any thermal crossover and, instead, scan the ground state landscape by tuning a non-thermal control parameter while staying at low temperatures. An added benefit of doing the latter is that the Fermi surface is only sharply defined at low temperatures, and studying the quantum phase transition through a non-thermal parameter variation allows for unambiguously detection of Fermi surface reconstruction.

$FeTe_{1-x}Se_x$ is a prototypical iron-based superconductor with the simplest crystal structure consisting of iron-chalcogen layers[39]. Recent studies have also revealed the existence of topological surface states and potential Majorana zero modes in this material platform[40–42]. The parent compound, FeTe, is an AFM metal[43–46]. With the isovalent substitution of Se on Te sites, superconductivity emerges, reaching a maximum T_c of 14.5 K in $FeTe_{0.56}Se_{0.44}$[46,47]. It is known that as-grown single crystals of $FeTe_{1-x}Se_x$ have a tendency to harbor interstitial excess iron, which leads to spin-glass behavior and incoherence in the low energy electronic spectra[48,49]. It has been shown that the excess Fe can be reduced or completely removed by annealing in either an oxygen or Te-vapor environment[50–53], which suppresses the spin-glass behavior and results in a phase diagram that bares a closer resemblance to that of iron pnictides[54].

In this work, we present systematic evidence for a reconstruction of the Fermi surface driven by orbital-dependent correlation effects in the $FeTe_{1-x}Se_x$ family of superconductors as the phase diagram is traversed non-thermally along the Se-substitution axis as well as along the temperature axis. Remarkably, strong reorganization of the Fermi surface is observed in the absence of any symmetry-breaking electronic order. We demonstrate how the more coherent d-orbitals, in particular, the d_{z^2} orbital, serve as a transparent means to visualize the suppression of the d_{xy} states at the Fermi energy by gradually appearing at the Fermi level as its hybridization with d_{xy} is turned off. In addition, we show that the Fermi surface reconstruction is accompanied by an orbital-dependent mass enhancement and signatures of a lower Hubbard band (LHB) as we tune from FeSe toward FeTe. Combined with the temperature axis, we not only arrive at a comprehensive phase diagram of the orbital-selectivity in $FeTe_{1-x}Se_x$, the understanding of which is discussed in connection with anomalies reported in measurements of the Hall coefficient, resistivity, and magnetic excitations, but also achieve a direct k-space visualization of the correlation-driven reconstruction of the electronic states near the Fermi energy.

Results

Fermi surface reconstruction. We begin by presenting a summary of our key results on the evolution of the Fermi surface along both the temperature and Se substitution axes of the $FeTe_{1-x}Se_x$ phase diagram (Fig. 1a). For simplicity, we refer to single crystals with the following Se content: $x = 0$, 0.11, 0.19, 0.28, 0.44 as FT, FTS11, FTS19, FTS28, FTS44, respectively. Starting from the familiar low temperature state of the optimally-substituted FTS44 (Fig. 1b), the Fermi surface dramatically changes compared to both

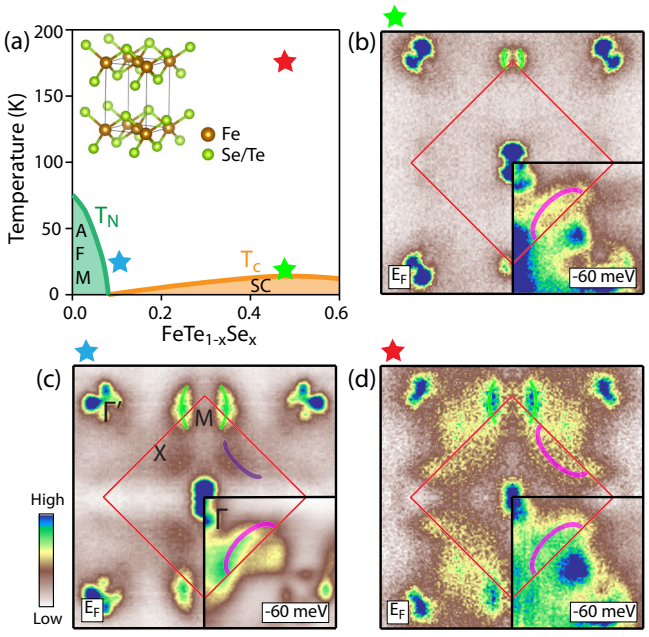

Fig. 1 Fermi surface evolution across the phase diagram of $FeTe_{1-x}Se_x$. **a** Phase diagram of $FeTe_{1-x}Se_x$ showing where the Fermi surfaces are measured. **b** Fermi surface and constant energy contour measured at −60 meV (lower right inset) for FTS44 taken at 18 K. **c**, **d** Same as (**b**) but taken on FTS11 at 24 K and FTS44 at 174 K, respectively. The red diamonds mark the 2-Fe Brillouin zone.

the low temperature Fermi surface of FTS11 just outside the magnetic ground state near FeTe (Fig. 1c) and its own high temperature state above the crossover into the OSMP (Fig. 1d)[15]. We note that in the region of the phase diagram spanning these three measurement points (Fig. 1a), there exists no known symmetry-breaking electronic orders. Yet, obvious changes in the Fermi surface can be observed. In low temperature FTS44, as previously reported[55–61], the Fermi surface consists of small hole pockets near the Brillouin zone (BZ) center (Γ) and electron pockets near the BZ corner (M). The wavevector difference between them matches the momentum transfer, where neutron spin resonance has been observed in the superconducting state[62]. In both the high temperature state of FTS44 and low temperature state of FTS11, the apparent fermiology has drastically changed in a similar fashion. The electron pocket at the M point is expanded while a new dominant arc-like spectral weight (marked in magenta and purple) appears along the BZ boundary centered at the X point. Interestingly, this arc-feature is already present in the constant energy contours at −60 meV for all three measurement points, in contrast to the Fermi surface. This observation suggests that the modifications along the substitution and temperature axes may have a similar origin. To understand this fermiology change, we examine the evolution across each axis of the phase diagram in turn.

We first present the measured Fermi surface of optimal FTS44 taken as a function of temperature from 18 K up to 174 K (Fig. 2a). Here we see the smooth evolution of the two changes previously mentioned: (i) expansion of the electron pockets at the M point, and (ii) emergence of an arc-like feature near the BZ boundary around X. While the Fermi surface is changing, we note that at −60 meV, no change is observed through this entire temperature range, where the spectral weight around X already appears at this binding energy even at the lowest temperature (Fig. 2b). This contrast suggests that the new feature observed near X at E_F emerges from higher binding energy when temperature is raised.

Next, we present the measured Fermi surface of $FeTe_{1-x}Se_x$ along the substitution-axis at low temperatures across the phase diagram (Fig. 3). To avoid complexity due to Fermi surface reconstruction from the bicollinear AFM phase of FT, we use the Fermi surface measured above the magnetic ordering temperature for FT in this comparison (Fig. 3a, the AFM state in FT is addressed in Supplementary Note 1). Hence across this comparison, there is no symmetry-breaking order. Yet, the same two qualitative changes can be observed with the decrease of the Se ratio (x): (i) expansion of the electron pockets near the M point, and (ii) emergence of the arc-like feature near the X point. As has been shown for the temperature evolution, the changes are limited to a small energy window near E_F, where the constant energy contours at −60 meV also show no obvious change with varying Se content (Fig. 3b). Comparing the Fermi surface across different Se content levels, the better resolved arc-like feature appears to evolve from a faint intensity near Γ, which is the spectral weight of the d_{xy} hole band in FTS44. This evolution is furthermore evident from the band dispersion measured along the Γ-X direction (Fig. 3c). As can be seen from both the dispersion images as well as the momentum distribution curve (MDC) stacks, a hole-like band emanating from the Γ point in FTS44 shifts toward the X point with decreasing x, eventually becoming a nearly vertical dispersion, giving rise to the arc-like feature that appears at E_F in FT. This also explains the observation that this arc-like feature is present already at high binding energy (−60 meV) across the different x presented in the phase diagram. From a set of detailed polarization-dependence measurements, the origin of this arc-like feature is identified to be predominantly of d_{z^2} orbital (see Supplementary Note 2 for photoemission matrix element analysis), which gradually evolves from high binding energy to E_F with decreasing x (Fig. 3d, e and f). We will discuss the spectral weight evolution later.

Orbital-dependent mass enhancement. The striking modifications to the low energy electronic states and fermiology via both temperature and the non-thermal substitution-axis in absence of any symmetry breaking phases call for an examination of the electronic correlations in this phase diagram. To determine the orbital-dependent correlation strength, we focus on the low-temperature (10 K) band renormalizations across the phase diagram near the BZ center. Along the high symmetry direction Γ-M, three hole-like bands are observed near E_F for all Se content which are better visualized from the second derivative plots (Fig. 3g). Consistent with previous results[57], these three bands from the innermost to the outermost are identified as dominantly d_{xz}, d_{yz}, and d_{xy}, respectively. As the phase diagram is traversed along the substitution-axis at 10 K, it is evident that the band curvature of the d_{yz} band does not vary strongly while that of the d_{xy} band flattens considerably with decreasing Se content. Since the effective mass for each band is proportional to the inverse of the band curvature, we can extract the orbital-dependent mass enhancement from a parabolic fitting of each band. The mass enhancement obtained from the ratio between the fitted effective mass m^* to that of first-principle calculations m_{DFT} is plotted as a function of Se content in Fig. 3h, consistent with the trend from previous results for higher Se content[61,63]. First, the mass enhancement of 40 is unusually large for 3d-electrons near the occupancy $n = 6$, even for the iron chalcogenides. Second, we observe an orbital-dependent band renormalization. The d_{xy} orbital has a much larger band renormalization factor than the d_{yz} orbital. Third, while the mass enhancement of the d_{yz} orbital rises slowly with decreasing Se ratio x, a divergent behavior of the mass enhancement for the d_{xy} orbital is observed with decreasing Se content. The inverse of the d_{xy} mass enhancement shows a linear trend versus Se ratio (Fig. 3h). These results strongly indicate that FeTe is in proximity to an OSMP ground state and further suggest

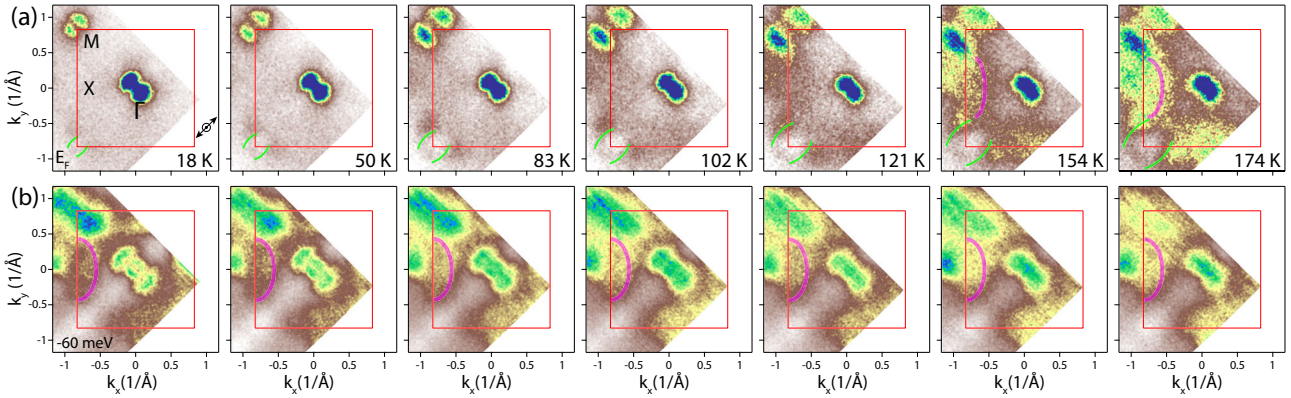

Fig. 2 Fermi surface evolution with temperature for FTS44. a Measured Fermi surfaces as temperature is varied between 18 K and 174 K. **b** Simultaneously measured constant energy contours at −60 meV showing no change as a function of temperature. Polarization is as marked in the left-most panel of (**a**) indicating an in-plane polarization along Γ-M with a finite out-of-plane component. The red squares mark the Brillouin zone of the 2-Fe unit cell.

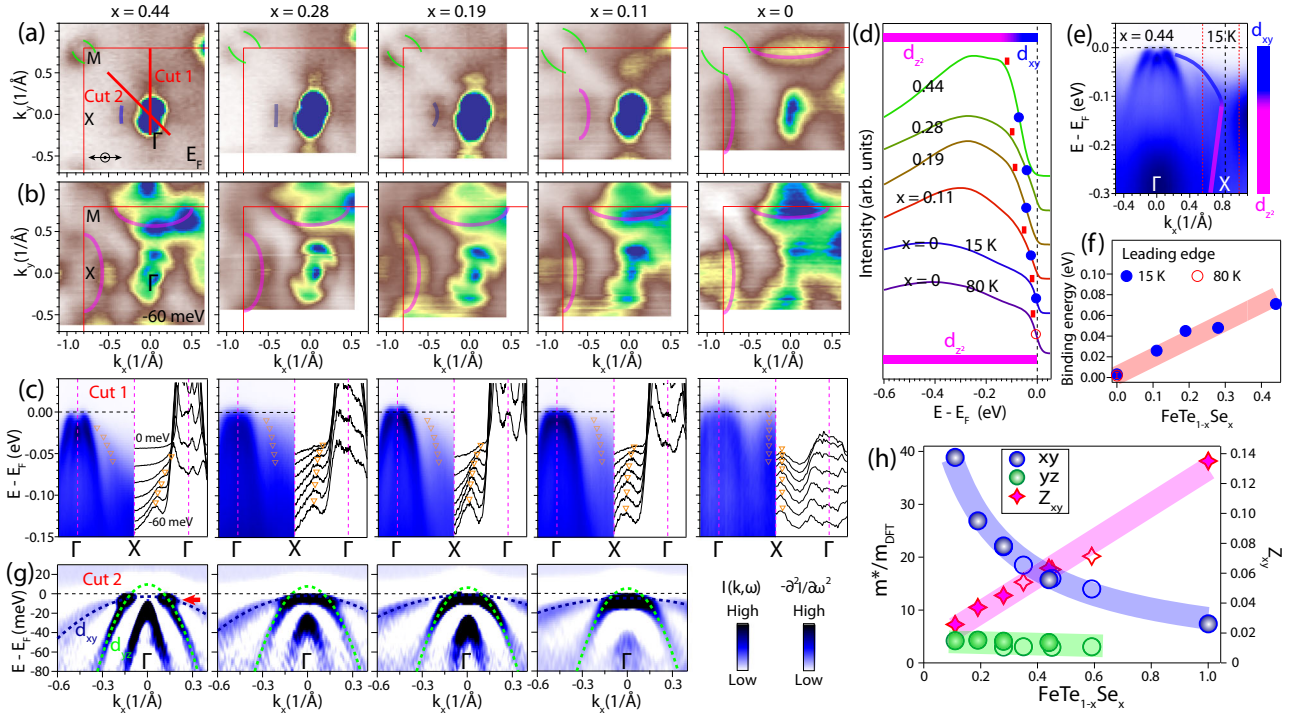

Fig. 3 Fermi surface evolution with Se ratio *x*. a Measured Fermi surfaces for different Se ratio x at 15 K except that for $x = 0$, which is measured at 80 K above its magnetic transition. **b** Simultaneously measured constant energy contours at −60 meV showing no change. **c** Corresponding band dispersions and momentum distribution curves (MDCs) along the Γ-X-Γ direction. The markers are peaks fitted from MDCs. The MDCs are for binding energies from 0 to 60 meV. **d** Integrated energy distribution curve (EDC) around X of $FeTe_{1-x}Se_x$ with the integral range marked by the red dashed lines in (**e**). The energy positions where the integrated EDCs show a maximum curvature are marked by the red bars. The leading edge marked by the blue and red circles represents the energy position where the EDC intensity is half of where at the maximum curvature. **e** Band dispersion of $FeTe_{0.56}Se_{0.44}$ at 15 K along the Γ-X-Γ direction. **f** Leading edge determined in (**d**) versus Se content of $FeTe_{1-x}Se_x$. **g** Band dispersions (second derivative) measured with 22 eV photons at 10 K along the Γ-M direction around the Brillouin zone center for different x. Parabolic fittings of the d_{yz} and d_{xy} hole bands are overlaid. The red arrow in left-most panel of (**g**) points at the hybridization of d_{yz} and d_{xy} orbitals. **h** Extracted band enhancement factor m^*/m_{DFT} for d_{yz} and d_{xy} plotted as a function of x represented by circles. The shaded lines are guides to the eyes. Diamond markers show the inverse of the d_{xy} mass enhancement where the shaded pink line is a linear fit. The empty markers are reproduced from Liu et al.[61].

that the evolution of the apparent fermiology is associated with the gradual disappearance of the d_{xy} spectral weight as x is reduced.

Visualizing the selective localization of d_{xy}-electrons via d_{z^2}-electrons. The orbital-dependent band renormalization, diverging d_{xy} effective mass, and modification of the Fermi surface, taken together, can be understood as manifestations of the tendency of the $FeTe_{1-x}Se_x$ system toward an OSMP with decreasing x. On the verge of Mott localization, the disappearance of the d_{xy} spectral weight near E_F results in a redistribution of the residual electronic states at E_F as the FeTe end of the phase diagram is approached. How does the diminishing d_{xy} weight at the Fermi level lead to the crossing of the d_{z^2} band through the

Fermi level? Qualitatively, we attribute this to the hybridization picture, which is believed to be important to the OSMP transition in the iron-based systems[64]. As symmetry dictates a nonzero hybridization matrix between the d_{xy} and d_{z^2} states near X, they are allowed to hybridize. Analogous to the appearance of a "large" Fermi surface in the *f*-electron heavy fermion metals, the itinerant d_{xy} states in $FeTe_{1-x}Se_x$ hybridize with the d_{z^2} states near X in the Fermi surface formation. As a result, the hybridization gap removes the d_{z^2} states from the Fermi level. However, just like the localization of the *f*-electrons in heavy fermion systems leads to a "small" Fermi surface of the *spd* conduction electrons, localizing the d_{xy}-electron states allows the d_{z^2}-electron states to cross the Fermi level near X.

To substantiate this qualitative picture, we have carried out calculations based on a five-orbital Hubbard model for $FeTe_{1-x}Se_x$ using the U(1) slave-spin method (for the method and the details of the calculation, see Supplementary Note 3 and 4). The substitution of larger Te atoms for smaller Se atoms increases the Fe-Se/Te bond length and decreases the Fe-Te/Se-Fe bond angle. The former effect increases the overall correlation strength by lengthening the dominant hopping path while the latter effect suppresses the effective hopping for the largely in-plane d_{xy} orbital more than that of the other orbitals, pushing the system toward an OSMP[6].

All salient features of our experimental observations presented are captured in this set of calculations, as shown by a direct comparison of the calculations for $x = 0.1$ and $x = 0.5$ (Fig. 4). Since density-functional theory (DFT) calculations (see Supplementary Note 3) do not capture well the observed dispersions near E_F, a U of 3 eV is used to be consistent with the experimentally observed band renormalizations (Supplementary Note 4). The projection onto the d_{xy} and d_{z^2} orbitals are shown in blue and magenta, respectively, for all calculations. In the strongly correlated metallic phase calculated for $x = 0.5$ (Fig. 4a), the d_{xy} dominated bands are strongly renormalized. When projected onto a Fermi surface mapping within a finite integration energy window about E_F, the flattened d_{xy} hole band intensity becomes largely incoherent, resulting in a faint large pocket spectra from the hole band around the Γ point (Fig. 4b). When the OSMP is entered, the band structure and Fermi surface are strongly reconstructed (Fig. 4c and d). The origin of this reconstruction is most apparent along the Γ-X direction. In the strongly correlated metallic phase (Fig. 4a), the strongly renormalized d_{xy} bands interrupt a highly dispersive d_{z^2} band near E_F, leading to very little d_{z^2} spectral weight in the Fermi surface. In the OSMP (Fig. 4c), the complete localization and gapping of the d_{xy} orbital from E_F frees the highly dispersive d_{z^2} band, which now crosses E_F, forming the pocket around the X point (Fig. 4d), consistent with our observed emergence of the arc-like feature around the X point. This fermiology is very consistent with that observed for the paramagnetic FeTe (right-most panel of Fig. 3a). Regarding the intermediate evolution of the band dispersions, in the regime approaching the OSMP, the d_{xy} bandwidth would narrow while its spectral weight diminishes, causing the hybridization between this d_{xy} band and the highly dispersive d_{z^2} band to decrease. This is consistent with our observed dispersions along the Γ-X direction, where the hole-like d_{xy} band in the low temperature state of FTS44 gradually evolves to the nearly vertical dispersion as the d_{z^2} band is recovered to E_F (Fig. 3c).

We can experimentally track the disappearance of this hybridization as a function of Se ratio. In Fig. 3d, we plot the integrated energy distribution curve (EDC) around the X point of $FeTe_{1-x}Se_x$ with different x (Fig. 3e). For FTS44, the integrated EDC shows a strong spectral weight suppression around E_F due to the hybridization between the d_{z^2} band and the d_{xy} band (Fig. 3e). Since the d_{xy} band strongly disperses away from X toward Γ, it largely falls outside the integration window. The integrated EDC within this narrow momentum range is dominated by the d_{z^2} spectral weight. The spectral suppression around E_F is therefore an indirect way to estimate the bandwidth of the d_{xy} band that hybridizes with the d_{z^2} band (Fig. 3d and e). As the d_{xy} band is increasingly renormalized, the spectral suppression in the integrated EDC will decrease as the d_{z^2} spectral weight fills toward E_F until the suppression completely

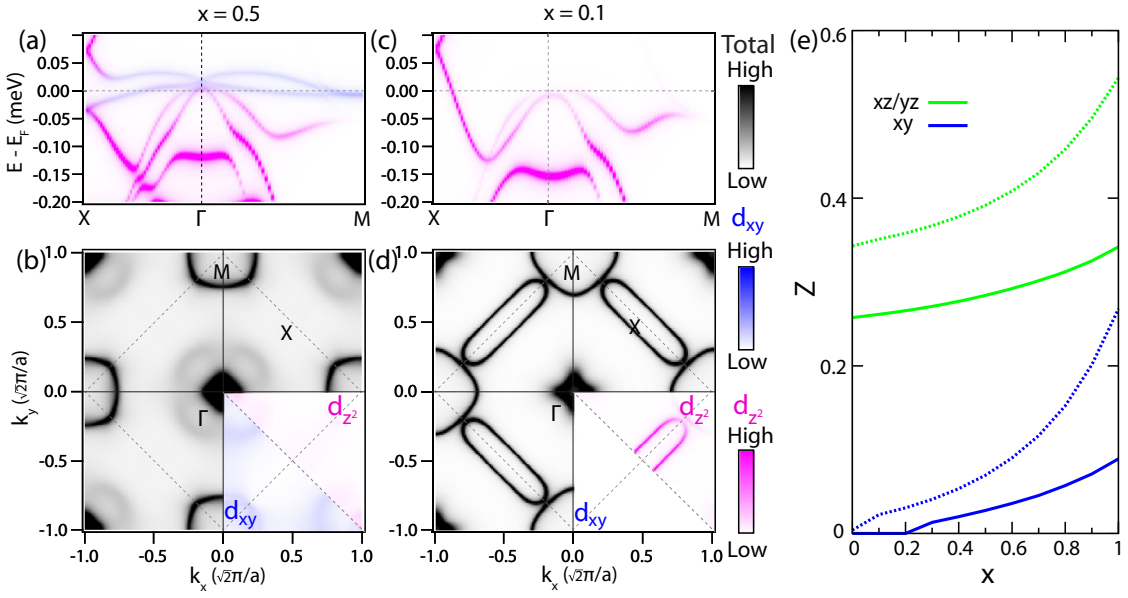

Fig. 4 Theoretical calculations of $FeTe_{1-x}Se_x$. **a** Calculated band structure projected onto different orbitals for the strongly correlated metallic phase in $FeTe_{0.5}Se_{0.5}$. The magenta intensity indicates d_{z^2} orbital character, whereas blue intensity the d_{xy} orbital. **b** Calculated Fermi surface for $FeTe_{0.5}Se_{0.5}$, where the lower right quadrant shows the d_{z^2} and d_{xy} intensity respectively. **c**, **d** Same as (**a**, **b**) but for the orbital-selective Mott phase $FeTe_{0.9}Se_{0.1}$. **e** Orbital-resolved coherence factor Z as a function of x. The solid line represents $U = 3$ eV and dashed line represents $U = 2.65$ eV. U denotes the intraorbital Coulomb repulsion.

disappears with the localization of the d_{xy} band in the OSMP. To capture the evolution of the spectral suppression with different x, we identify the leading edge of the integrated EDCs for samples with different Se content (Fig. 3d), and plot its energy as a function of Se content in Fig. 3f. The leading edge approaches the Fermi level with decreasing Se content, demonstrating that the gapped-out d_{z^2} spectral weight gradually fills in and forms the arc-like feature around X. Notably for FT, the leading edge shifts to E_F, indicating that it is in the OSMP at both 80 K and 15 K.

Besides the appearance of the arc-feature, the calculated d_{xz}/d_{yz} electron pocket enlarges, as observed experimentally, to compensate the hole pocket formed by the nearly vertical band around X. As a function of x, the calculated coherence factor, Z, for the d_{xz}/d_{yz} orbital is compared to that of the d_{xy} orbital (Fig. 4e), where localization of the d_{xy} orbital appears for $x < 0.2$ with $U \sim 3$ eV. We note that, the selective localization of the d_{xy} states also causes the suppression of their hybridization with d_{xz}/d_{yz} states. However, because the d_{z^2}-electron states are considerably more dispersive and gapped-out from E_F due to the hybridization with d_{xy}, they serve as an especially transparent diagnostic of the OSMP in the way of Fermi surface reconstruction (Fig. 4b, d).

Discussion

Finally, taking all the results together, we arrive at the phase diagram for the $FeTe_{1-x}Se_x$ material family (Fig. 5). While previous results[15] indicate that for an optimally substituted compound at $x = 0.44$, the OSMP can be reached via raised temperature at a characteristic temperature of 110 K, our observations reported here show that in the low temperature limit, the replacement of Se by Te also leads the material system toward the OSMP. This is supported by spectroscopic evidence of strongly orbital-selective band renormalization where the d_{xy} effective mass tends toward a divergent behavior as the FeTe end is approached. Concomitantly, spectral weight from other orbitals redistribute near the E_F to replace the diminishing d_{xy} spectral weight. The characteristic crossover temperature for the OSMP therefore decreases with decreasing x. This is confirmed by our measurement for a sample with $x = 0.25$, where the temperature identified by the disappearance of d_{xy} is measured to be 70 K (Supplementary Note 5). We note that considering the bandwidth of the d_{xy} orbital (≥ 30 meV, 350 K), the observed disappearance of the d_{xy} spectral weight as a function of Se ratio measured at 10 K cannot be caused by the thermal broadening effect, but rather due to the narrowing of the d_{xy} bandwidth as the system enters into the OSMP.

Our understanding of the evolution from an orbital-dependent correlated metallic phase to an OSMP across the $FeTe_{1-x}Se_x$ phase diagram as observed from ARPES is also consistent with results reported by other probes. It has been reported that the compensated parent compounds of multi-band FeSC exhibit a negative Hall coefficient, R_H, due to the dominance of the electron mobility. This is observed in isovalent-substituted $BaFe_2(As,P)_2$, where across the entire phase diagram, R_H remains negative[65,66]. For $FeTe_{1-x}Se_x$, however, there is a systematic change that varies as a function of substitution[67]. This is clearly shown in the measurement over the phase diagram of Te-vapor treated $FeTe_{1-x}Se_x$ (Fig. 5)[67]. Contrary to the behavior in $BaFe_2(As,P)_2$, Hall resistivity measurements on $FeTe_{1-x}Se_x$ exhibit a maximum and a subsequent sign-change at lower temperatures while the total charge carriers remain neutral[67]. This turn-over behavior marked by the maximum indicates the onset of a competing behavior (Fig. 5a). One interpretation of the negative Hall coefficient in the iron pnictides is the (π, π) spin fluctuations that make the hole carriers behave like electron carriers in the Hall measurements[68]. The localization of the d_{xy} orbital would change the fermiology

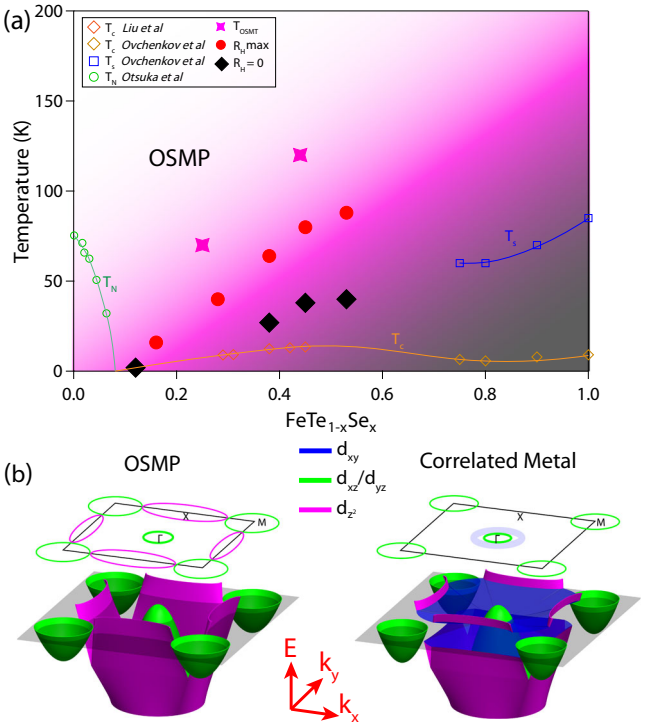

Fig. 5 Phase diagram of $FeTe_{1-x}Se_x$. **a** T_N[69], T_s[78] and T_c[46,78] represent the bi-collinear spin-density wave transition, tetragonal to orthorhombic structural transition, and superconducting transition adapted from previous reports. The temperatures for Hall resistivity (R_H) maximum positions and $R_H = 0$ are extracted from the Hall resistivity measurements[67]. T_{OSMT} is the temperature at which the photoemission spectral weight of d_{xy} orbital is observed to vanish (Supplementary Note 5). OSMT represents orbital-selective Mott transition. The background with gradient color suggests the orbital-selective Mott phase (OSMP) crossover. **b** Schematics showing the key features of the band structure of $FeTe_{1-x}Se_x$ in the OSMP and correlated metal phase respectively. The disappearance of band hybridization due to the complete incoherence of d_{xy} orbital is responsible for the Fermi surface reconstruction.

away from the nesting condition associated with the (π, π) spin fluctuations. This in turn suppresses the (π, π) spin fluctuations, which reduces the negative contribution to the Hall coefficient. This characteristic temperature scale extracted from R_H exhibits a similar trend with Se ratio x, similar to T_{OSMT}, which is the temperature where the spectral weight of d_{xy} orbital vanishes with increasing temperature.

We also note that in a recent magneto-transport measurement, such coherent-incoherent crossover is also reported[69]. It has also been pointed out that this coherent-incoherent crossover temperature scale of the d_{xy} orbital is coupled to the B_{2g} nematic susceptibility measured by elastoresistance, and hence suggests the potential important role played by the d_{xy} orbital to nematicity in the FeSC[67].

Previous studies of both Dynamic Mean Field Theory and ARPES have also identified the incoherent spectral weight in the high binding energy regime of FeSe as the LHB, indicating the presence of strong electron correlations in this material system[70,71]. The incoherent feature has also been observed by our ARPES measurements as well as theoretical calculations (see Supplementary Note 6).

Further connection between our ARPES report of OSMP and magnetic excitations via inelastic neutron scattering can also be made. It has been reported that along both the temperature axis[72]

and substitution axis[73], low energy magnetic excitations have been observed to change from a commensurate U-shape to a double-rod shape in the absence of any symmetry-breaking orders[42]. The trend of such behavior is consistent with the observation of the modification of the low energy electronic states along both axes as we have reported, suggesting a common origin.

An OSMP is depicted by the coexistence of localized and itinerant orbitals within one material system[28,31,32]. Across the $FeTe_{1-x}Se_x$ phase diagram, we observe a large dynamic range of the relative coherence of the localized d_{xy} orbital to that of the other itinerant Fe 3d orbitals. In our work, we have discovered a surprisingly transparent way for the d_{z^2} electrons to serve as a diagnostic for the selective localization of the d_{xy} electron states as the OSMP emerges (Fig. 5b). To achieve an OSMP in $FeTe_{1-x}Se_x$, besides the strong electron-electron interaction, three other ingredients are necessary: (i) Crystal field splitting that separates the d_{xy} orbital from d_{xz}/d_{yz}; (ii) Bare bandwidth of the d_{xy} orbital being narrower than that of the d_{xz}/d_{yz} orbitals; (iii) Suppression of the inter-orbital interactions due to Hund's J[13]. Our systematic measurement of the fermiology across the $FeTe_{1-x}Se_x$ phase diagram establishes the first example to the best of our knowledge amongst the FeSCs where the low energy electronic states are drastically modified due to electron correlation effects, establishing this most correlated FeSC family as an anchoring point between the more itinerant iron pnictides and the more localized cuprates. More generally, the correlation-driven electron reconstruction implies that the Fe 3d-electrons are at the boundary between delocalization and localization in an orbital-selective way. As such, the delocalization-localization physics anchors the orbital-selective correlations that have been observed in essentially all the iron-chalcogenide superconductors, including the monolayer FeSe on $SrTiO_3$ that holds the record of superconducting T_c in the FeSCs, and in many iron pnictide superconductors[12,15]. Consequently, the electrons' localization-delocalization tendency, along with their proximity to electronic orders, is important both to generating the unusual properties of the normal state and to driving the high-temperature superconductivity.

Methods

Sample growth and characterization. Our high quality $Fe_yTe_{1-x}Se_x$ single crystal series were synthesized using the flux method[74]. The FeSe single crystal was synthesized using chemical vapor transport[75]. The excess Fe in all as-grown $Fe_{y-}Te_{1-x}Se_x$ single crystals was reduced by annealing in a Te-vapor atmosphere[76,77]. Crystals with the following Se content were used: $x = 0$, 0.11, 0.19, 0.28, 0.44. The Fe contents of the cleaved surface of these crystals were measured via energy dispersive x-ray spectroscopy following the ARPES measurements and determined to be $y = 1.08$, 1.07, 1.03, 1.01, and 1.00, respectively.

ARPES measurements. ARPES experiments were performed at beamlines 5–4 and 5–2 of the Stanford Synchrotron Radiation Light source with R4000 and DA30 electron analyzers, respectively, beamlines 4.0.3 and 10.0.1 of the Advanced Light Source with R8000 and R4000 electron analyzers, respectively, and the QMSC beamline of the Canadian Light Source with an R4000 electron analyzer. Results were reproduced at all facilities. The angular resolution was set to 0.3° or better. The total energy resolution was set to 15 meV or better. All samples were cleaved in-situ below 15 K and all the measurements were conducted in ultra-high vacuum with a base pressure lower than 5×10^{-11} Torr using 72 eV photons unless otherwise noted.

Data availability

All data needed to evaluate the conclusions are present in the paper and supplementary materials. Additional data are available from the corresponding author on reasonable request.

Received: 12 October 2021; Accepted: 23 December 2021;
Published online: 26 January 2022

References

1. Paglione, J. & Greene, R. L. High-temperature superconductivity in iron-based materials. *Nat. Phys.* **6**, 645–658 (2010).
2. Wang, F. & Lee, D.-H. The Electron-Pairing Mechanism of Iron-Based Superconductors. *Science* **332**, 200–204 (2011).
3. Keimer, B., Kivelson, S. A., Norman, M. R., Uchida, S. & Zaanen, J. From quantum matter to high-temperature superconductivity in copper oxides. *Nature* **518**, 179–186 (2015).
4. Lee, P. A., Nagaosa, N. & Wen, X. G. Doping a Mott insulator: physics of high-temperature superconductivity. *Rev Modern Phys.* **78**, 17–85 (2006).
5. Yin, Z. P., Haule, K. & Kotliar, G. Kinetic frustration and the nature of the magnetic and paramagnetic states in iron pnictides and iron chalcogenides. *Nat. Mater.* **10**, 932–935 (2011).
6. Yi, M., Zhang, Y., Shen, Z.-X. & Lu, D. Role of the orbital degree of freedom in iron-based superconductors. *npj Quant. Mater.* **2**, 57 (2017).
7. Chen, S.-D. et al. Incoherent strange metal sharply bounded by a critical doping in Bi2212. *Science* **366**, 1099–1102 (2019).
8. de la Cruz, C. et al. Magnetic order close to superconductivity in the iron-based layered $LaO_{1-x}F_xFeAs$ systems. *Nature* **453**, 899–902 (2008).
9. Yi, M. et al. Symmetry-breaking orbital anisotropy observed for detwinned $Ba(Fe_{1-x}Co_x)_2As_2$ above the spin density wave transition. *Proc. Natl Acad. Sci.* **108**, 6878–6883 (2011).
10. Sobota, J. A., He, Y. & Shen, Z.-X. Angle-resolved photoemission studies of quantum materials. *Rev. Modern Phys.* **93**, 025006 (2021).
11. Qazilbash, M. M. et al. Electronic correlations in the iron pnictides. *Nat. Phys.* **5**, 647–650 (2009).
12. de' Medici, L., Giovannetti, G. & Capone, M. Selective Mott Physics as a Key to Iron Superconductors. *Phys. Rev. Lett.* **112**, 177001 (2014).
13. Si, Q., Yu, R. & Abrahams, E. High-temperature superconductivity in iron pnictides and chalcogenides. *Nat. Rev. Mater.* **1**, 16017 (2016).
14. Yin, Z. P., Haule, K. & Kotliar, G. Fractional power-law behavior and its origin in iron-chalcogenide and ruthenate superconductors: Insights from first-principles calculations. *Phys. Rev. B* **86**, 195141 (2012).
15. Yi, M. et al. Observation of universal strong orbital-dependent correlation effects in iron chalcogenides. *Nat. Commun.* **6**, 7777 (2015).
16. Pu, Y. J. et al. Temperature-induced orbital selective localization and coherent-incoherent crossover in single-layer FeSe/Nb:$BaTiO_3$/$KTaO_3$. *Phys. Rev. B* **94**, 115146 (2016).
17. Dai, P., Hu, J. & Dagotto, E. Magnetism and its microscopic origin in iron-based high-temperature superconductors. *Nat. Phys.* **8**, 709–718 (2012).
18. Li, J. et al. Spin-Orbital-Intertwined Nematic State in FeSe. *Phys. Rev. X* **10**, 011034 (2020).
19. Li, Y. et al. Dynamic Spin-Lattice Coupling and Nematic Fluctuations in NaFeAs. *Phys. Rev. X* **8**, 021056 (2018).
20. Song, Y. et al. Unusual suppression of a spin resonance mode by magnetic field in underdoped $NaFe_{1-x}Co_xAs$: evidence for orbital-selective pairing. *Phys. Rev. B* **98**, 064507 (2018).
21. Tam, D. W. et al. Orbital selective spin waves in detwinned NaFeAs. *Phys. Rev. B* **102**, 054430 (2020).
22. Zhao, H. et al. Nematic transition and nanoscale suppression of superconductivity in Fe(TeSe). *Nature Physics* **17**, 903–908 (2021).
23. De'Medici, L., Georges, A. & Biermann, S. Orbital-selective Mott transition in multiband systems: Slave-spin representation and dynamical mean-field theory. *Phys. Rev. B* **72**, 205124 (2005).
24. Ferrero, M. et al. Pseudogap opening and formation of Fermi arcs as an orbital-selective Mott transition in momentum space. *Phys. Rev. B* **80**, 064501 (2009).
25. Greger, M., Kollar, M. & Vollhardt, D. Emergence of a Common Energy Scale Close to the Orbital-Selective Mott Transition. *Phys. Rev. Lett.* **110**, 046403 (2013).
26. Yu, R. & Si, Q. Orbital-Selective Mott Phase in Multiorbital Models for Alkaline Iron Selenides $K_{1-x}Fe_{2-y}Se_2$. *Phys. Rev. Lett.* **110**, 146402 (2013).
27. Georges, A., de' Medici, L. & Mravlje, J. Strong Correlations from Hund's Coupling. *Ann. Rev. Condensed Matter Phys.* **4**, 137–178 (2013).
28. Anisimov, V., Nekrasov, I., Kondakov, D., Rice, T. & Sigrist, M. Orbital-selective Mott-insulator transition in $Ca_{2-x}Sr_xRuO_4$. *Eur. Phys. J. B* **25**, 191–201 (2002).
29. Neupane, M. et al. Observation of a Novel Orbital Selective Mott Transition in $Ca_{1.8}Sr_{0.2}RuO_4$. *Phys. Rev. Lett.* **103**, 097001 (2009).
30. Kim, M. et al. Observation of Kondo hybridization with an orbital-selective Mott phase in 4d $Ca_{2-x}Sr_xRuO_4$. *arXiv* **2102**, 09760 (2021).
31. Mukherjee, S. et al. Tuning a strain-induced orbital selective Mott transition in epitaxial VO_2. *Phys. Rev. B* **93**, 241110 (2016).
32. Qiao, S. et al. Mottness Collapse in 1T-$TaS_{2-x}Se_x$ Transition-Metal Dichalcogenide: an Interplay between Localized and Itinerant Orbitals. *Phys. Rev. X* **7**, 041054 (2017).
33. Shimoyamada, A. et al. Strong Mass Renormalization at a Local Momentum Space in Multiorbital $Ca_{1.8}Sr_{0.2}RuO_4$. *Phys. Rev. Lett.* **102**, 086401 (2009).

34. Saeki, K. et al. Band dispersion near the Fermi level for VO_2 thin films grown on TiO_2 (001) substrates. *Phys. Rev. B* **80**, 125406 (2009).
35. Ang, R. et al. Superconductivity and bandwidth-controlled Mott metal-insulator transition in 1 T-$TaS_{2-x}Se_x$. *Phys. Rev. B* **88**, 115145 (2013).
36. Sutter, D. et al. Hallmarks of Hunds coupling in the Mott insulator Ca_2RuO_4. *Nat. Commun.* **8**, 15176 (2017).
37. Muraoka, Y. et al. Fermi surface topology in a metallic phase of VO_2 thin films grown on TiO_2(001) substrates. *Sci. Rep.* **8**, 17906 (2018).
38. Yi, M. et al. Observation of temperature-induced crossover to an orbital-selective mott phase in $A_xFe_{2-y}Se_2$ (A = K, Rb) superconductors. *Phys. Rev. Lett.* **110**, 067003 (2013).
39. Hsu, F.-C. et al. Superconductivity in the PbO-type structure α-FeSe. *Proc. Natl Acad. Sci.* **105**, 14262–14264 (2008).
40. Zhang, P. et al. Observation of topological superconductivity on the surface of an iron-based superconductor. *Sciences* **360**, 182–186 (2018).
41. Wang, D. et al. Evidence for Majorana bound states in an iron-based superconductor. *Sciences* **362**, 333–335 (2018).
42. Li, Y. et al. Electronic properties of the bulk and surface states of $Fe_{1+y}Te_{1-x}Se_x$. *Nat. Mater.* **20**, 1221–1227 (2021).
43. Fruchart, D. et al. Structure antiferromagnetique de $Fe_{1.125}Te$ accompagnee d'une deformation monoclinique. *Mater. Res. Bull.* **10**, 169–174 (1975).
44. Bao, W. et al. Tunable ($\delta\pi$, $\delta\pi$)-Type Antiferromagnetic Order in α-Fe(Te,Se) Superconductors. *Phys. Rev. Lett.* **102**, 247001 (2009).
45. Li, S. et al. First-order magnetic and structural phase transitions in $Fe_{1+y}Se_xTe_{1-x}$. *Phys. Rev. B* **79**, 054503 (2009).
46. Liu, T. J. et al. From (π,0) magnetic order to superconductivity with (π,π) magnetic resonance in $Fe_{1.02}Te_{1-x}Se_x$. *Nat. Mater.* **9**, 716–720 (2010).
47. Martinelli, A. et al. From antiferromagnetism to superconductivity in $Fe_{1+y}Te_{x-x}Se_x$ ($0 \le x \le 0.20$):Neutron powder diffraction analysis. *Phys. Rev. B* **81**, 094115 (2010).
48. Katayama, N. et al. Investigation of the Spin-Glass Regime between the Antiferromagnetic and Superconducting Phases in $Fe_{1+y}Se_xTe_{1-x}$. *J. Phys. Soc. Japan* **79**, 113702 (2010).
49. Ieki, E. et al. Evolution from incoherent to coherent electronic states and its implications for superconductivity in $FeTe_{1-x}Se_x$. *Phys. Rev. B* **89**, 140506 (2014).
50. Sun, Y. et al. Evolution of superconducting and transport properties in annealed $FeTe_{1-x}Se_x$ ($0.1 \le x \le 0.4$) multiband superconductors. *Superconductor Sci. Technol.* **28**, 044002 (2015).
51. Dong, C. et al. Revised phase diagram for the $FeTe_{1-x}Se_x$ system with fewer excess Fe atoms. *Phys. Rev. B* **84**, 224506 (2011).
52. Lin, W. et al. Role of chalcogen vapor annealing in inducing bulk superconductivity in $Fe_{1+y}Te_{1-x}Se_x$. *Phys. Rev. B* **91**, 060513 (2015).
53. Sun, Y. et al. Dynamics and mechanism of oxygen annealing in $Fe_{1+y}Te_{0.6}Se_{0.4}$ single crystal. *Sci. Rep.* **4**, 4585 (2015).
54. Sun, Y., Yamada, T., Pyon, S. & Tamegai, T. Influence of interstitial Fe to the phase diagram of $Fe_{1+y}Te_{1-x}Se_x$ single crystals. *Sci. Rep.* **6**, 32290 (2016).
55. Chen, F. et al. Electronic structure of $Fe_{1.04}Te_{0.66}Se_{0.34}$. *Phys. Rev. B* **81**, 014526 (2010).
56. Tamai, A. et al. Strong electron correlations in the normal state of the iron-based $FeSe_{0.42}Te_{0.58}$ superconductor observed by angle-resolved photoemission spectroscopy. *Phys. Rev. Lett.* **104**, 097002 (2010).
57. Nakayama, K. et al. Angle-resolved photoemission spectroscopy of the iron-chalcogenide superconductor $Fe_{1.03}Te_{0.7}Se_{0.3}$: Strong coupling behavior and the universality of interband scattering. *Phys. Rev. Lett.* **105**, 197001 (2010).
58. Miao, H. et al. Isotropic superconducting gaps with enhanced pairing on electron Fermi surfaces in $FeTe_{0.55}Se_{0.45}$. *Phys. Rev. B* **85**, 094506 (2012).
59. Okazaki, K. et al. Evidence for a $cos(4\phi)$ Modulation of the Superconducting Energy Gap of Optimally Doped $FeTe_{0.6}Se_{0.4}$ Single Crystals Using Laser Angle-Resolved Photoemission Spectroscopy. *Phys. Rev. Lett.* **109**, 237011 (2012).
60. Lubashevsky, Y., Lahoud, E., Chashka, K., Podolsky, D. & Kanigel, A. Shallow pockets and very strong coupling superconductivity in $FeSe_xTe_{1-x}$. *Nat. Phys.* **8**, 309–312 (2012).
61. Liu, Z. K. et al. Experimental observation of incoherent-coherent crossover and orbital-dependent band renormalization in iron chalcogenide superconductors. *Phys. Rev. B* **92**, 235138 (2015).
62. Qiu, Y. et al. Spin Gap and Resonance at the Nesting Wave Vector in Superconducting $FeSe_{0.4}Te_{0.6}$. *Phys. Rev. Lett.* **103**, 067008 (2009).
63. Maletz, J. et al. Unusual band renormalization in the simplest iron-based superconductor $FeSe_{1-x}$. *Phys. Rev. B* **89**, 220506 (2014).
64. Yu, R. & Si, Q. Orbital-selective Mott phase in multiorbital models for iron pnictides and chalcogenides. *Phys. Rev. B* **96**, 125110 (2017).
65. Fang, L. et al. Roles of multiband effects and electron-hole asymmetry in the superconductivity and normal-state properties of $Ba(Fe_{1-x}Co_x)_2As_2$. *Phys. Rev. B* **80**, 140508 (2009).
66. Kasahara, S. et al. Evolution from non-Fermi- to Fermi-liquid transport via isovalent doping in $BaFe_2(As_{1-x}P_x)_2$ superconductors. *Phys. Rev. B* **81**, 184519 (2010).
67. Jiang, Q. et al. Nematic Fluctuations in an Orbital Selective Superconductor $Fe_{1+y}Te_{1-x}Se_x$. *arXiv* **2006**, 15887 (2020).
68. Fanfarillo, L., Cappelluti, E., Castellani, C. & Benfatto, L. Unconventional Hall Effect in Pnictides from Interband Interactions. *Phys. Rev. Lett.* **109**, 096402 (2012).
69. Otsuka, T. et al. Incoherent-coherent crossover and the pseudogap in Te-annealed superconducting $Fe_{1+y}Te_{1-x}Se_x$ revealed by magnetotransport measurements. *Phys. Rev. B* **99**, 184505 (2019).
70. Evtushinsky, D. V. et al. Direct observation of dispersive lower Hubbard band in iron-based superconductor FeSe. *arXiv* **1612**, 02313 (2016).
71. Watson, M. D. et al. Formation of Hubbard-like bands as a fingerprint of strong electron-electron interactions in FeSe. *Phys. Rev. B* **95**, 081106 (2017).
72. Xu, Z. et al. Low-energy magnetic excitations from the Fe_{1+y-z}(Ni/Cu)$_z$$Te_{1-x}Se_x$ system. *Phys. Rev. B* **89**, 174517 (2014).
73. Christianson, A. D. et al. Doping dependence of the spin excitations in the Fe-based superconductors $Fe_{1+y}Te_{1-x}Se_x$. *Phys. Rev. B* **87**, 224410 (2013).
74. Liu, T. J. et al. Charge-carrier localization induced by excess Fe in the superconductor $Fe_{1+y}Te_{1-x}Se_x$. *Phys. Rev. B* **80**, 174509 (2009).
75. Chen, T. et al. Anisotropic spin fluctuations in detwinned FeSe. *Nat. Mater.* **18**, 709–716 (2019).
76. Xu, Z. et al. Coexistence of superconductivity and short-range double-stripe spin correlations in Te-vapor annealed $FeTe_{1-x}Se_x$ (x≤0.2). *Phys. Rev. B* **97**, 214511 (2018).
77. Koshika, Y. et al. Effects of Annealing under Tellurium Vapor for $Fe_{1.03}Te_{0.8}Se_{0.2}$ Single Crystals. *J. Phys. Soc. apan* **82**, 023703 (2013).
78. Ovchenkov, Y. A. et al. Nematic properties of $FeSe_{1-x}Te_x$ crystals with a low Te content. *arXiv* **1909**, 00711 (2019).

Acknowledgements

We are thankful to Yu He for enlightening discussions. Parts of the research were performed at the Advanced Light Source and the Stanford Synchrotron Radiation Light source, both operated by the Office of Basic Energy Sciences (BES), U.S. Department of Energy (DOE). Work at University of California, Berkeley and Lawrence Berkeley National Laboratory was funded by the U.S. Department of Energy, Office of Science, Office of Basic Energy Sciences, Materials Sciences and Engineering Division under Contract No. DE-AC02-05-CH11231 within the Quantum Materials Program (KC2202) and the Office of Basic Energy Sciences. Part of the research described in this work was performed at the Canadian Light Source, a national research facility of the University of Saskatchewan, which is supported by Canada Foundation for Innovation (CFI), the Natural Sciences and Engineering Research Council of Canada (NSERC), the National Research Council (NRC), the Canadian Institutes of Health Research (CIHR), the Government of Saskatchewan, and the University of Saskatchewan. The ARPES work at Rice University was supported by the Robert A. Welch Foundation Grant No. C-2024, the Alfred P. Sloan Foundation, the Gordon and Betty Moore Foundation's EPiQS Initiative through grant No. GBMF9470, and the US DOE, under Award No. DE-SC0021421. The materials synthesis efforts at Rice are supported by the US DOE, BES, under Contract No. DE-SC0012311 and the Robert A. Welch Foundation, Grant No. C-1839 (P.D.). Theory work at Rice University is supported by the U.S. DOE, Office of Science, BES, under Award No. DE-SC0018197, and by the Robert A. Welch Foundation Grant No. C-1411. Theory work at Renmin University has in part been supported by the National Science Foundation of China Grant No. 11674392, Ministry of Science and Technology of China, National Program on Key Research Project Grant No.2016YFA0300504 and Research Funds of Renmin University of China Grant No. 18XNLG24 (R.Y.). Theory work at Los Alamos was carried out under the auspices of the U.S. Department of Energy National Nuclear Security Administration under Contract No. 89233218CNA000001, and was supported by the LANL LDRD Program. Work at the University of Washington was supported by NSF MRSEC at UW (DMR1719797). Work at Sun Yat-Sen University was supported by the National Natural Science Foundation of China (Grant No. 11904414) and National Key Research and Development Program of China (No. 2019YFA0705702). Work at Brookhaven is supported by the Office of BES, Division of Materials Sciences and Engineering, U.S. DOE under contract Nos. DE-AC02-98CH10886 and DE-SC00112704. This research was undertaken thanks, in part, to funding from the Max Planck-UBC-UTokyo Center for Quantum Materials and the Canada First Research Excellence Fund, Quantum Materials and Future Technologies Program.

Author contributions

M.Y. and R.J.B. proposed and designed the research. M.Y., J.H., M.W., J.S.O., and H.W. carried out the ARPES measurements with the help of D.L., M.H., J.D.D., S.-K.M., M.M., T.M.P., S.G., S.Z., and A.D. The ARPES data were analyzed by J.H. and M.Y. Single crystals of $FeTe_{1-x}Se_x$ were synthesized by Z.X. and G.G. FeSe single crystals were synthesized by T.C. under the guidance of P.D. Theoretical calculations were carried out by R.Y., J.-X.Z., and Q.S. Hall measurements were carried out by Q.J. and J.-H.C. J.H. and M.Y. wrote the paper with input from all co-authors. M.Y. and R.J.B. oversaw the project.

Competing interests

The authors declare no competing interests. M.Y. is an Editorial Board Member for Communications Physics, but was not involved in the editorial review of, or the decision to publish this paper.

Additional information

Supplementary information The online version contains supplementary material available at https://doi.org/10.1038/s42005-022-00805-6.

Correspondence and requests for materials should be addressed to Robert J. Birgeneau or Ming Yi.

Peer review information *Communications Physics* thanks Ilija Zeljkovic and the other, anonymous, reviewer(s) for their contribution to the peer review of this work.

Reprints and permission information is available at http://www.nature.com/reprints

Publisher's note Springer Nature remains neutral with regard to jurisdictional claims in published maps and institutional affiliations.